Applied Catalysis B: Environmental 221 (2018) 510–520

Contents lists available at ScienceDirect

Applied Catalysis B: Environmental

journal homepage: www.elsevier.com/locate/apcatb

Novel ternary photocatalyst of single atom-dispersed silver and carbon quantum dots co-loaded with ultrathin g-C_3N_4 for broad spectrum photocatalytic degradation of naproxen

Fengliang Wang[a], Yingfei Wang[a], Yiping Feng[a], Yongqin Zeng[a], Zhijie Xie[a], Qianxin Zhang[a], Yuehan Su[a], Ping Chen[b], Yang Liu[c], Kun Yao[a], Wenying Lv[a], Guoguang Liu[a,*]

[a] School of Environmental Science and Engineering, and Institute of Environmental Health and Pollution Control, Guangdong University of Technology, Guangzhou, 510006, China

[b] School of Environment, Tsinghua University, Beijing 100084, China

[c] Faculty of Environmental & Biological Engineering, Guangdong University of Petrochemical Technology, Maoming, 525000, China

ARTICLE INFO

Keywords:
Graphitic carbon nitride
Carbon quantum dots
Single atom-dispersed silver
Broad-spectrum
NPX

ABSTRACT

The development of highly efficient photocatalysts with broad spectrum light response is a primary goal in the photocatalysis domain. Here we report on a novel ternary photocatalyst comprised of single atom-dispersed silver and carbon quantum dots, co-loaded with ultrathin g-C_3N_4 (SDAg-CQDs/UCN), which exhibited a highly enhanced photoresponse and broad-spectrum (UV, visible, and near-infrared light) photocatalytic activity. The content of 1.0 wt% of CQDs and 3.0 wt% of Ag resulted in a 10-fold higher reaction rate than that of UCN under visible light irradiation. This improved broad-spectrum photocatalytic performance may be attributed to the surface plasmon resonance effect of Ag, up-converted fluorescent properties of CQDs, narrowed energy gap, as well as the electron separation and transfer capacity of both the Ag and CQDs. An electron spin resonance (ESR) technique, and reactive species (RS) scavenging experiments indicated that $^1O_2$ and $O_2\cdot^-$ were the dominant active species involved in the degradation of naproxen (NPX). Product identification and reaction site prediction revealed that the photocatalytic degradation of NPX included decarboxylation, hydroxylation, as well as the opening of the naphthalene ring. Mineralization experiments indicated that NPX and its degradation products would be finally transformed into CO_2 and H_2O. Reactions in different water matrices indicated that SDAg-CQDs/UCN can be effectively employed for the degradation of NPX under ambient water conditions. Therefore, SDAg-CQDs/UCN offers a new strategy for the broad-spectrum utilization of solar light and provides a promising method for the remediation of water contamination.

1. Introduction

Semiconductor based photocatalysis is considered to be an effective approach for resolving the energy crisis and environmental pollution issues [1–3]. Regarding the utilization of solar energy, there is an increasing urgency to explore new and efficient semiconductor photocatalysts that may utilize the entire solar light spectrum, spanning ultraviolet (UV) to near-infrared (NIR) toward the achievement of efficient broad-spectrum photocatalytic performance [4]. As a metal-free organic polymeric semiconductor, graphitic carbon nitride (g-C_3N_4) has been widely used in solar-initiated photocatalytic hydrogen evolution and the photo-reduction of CO_2 and organic contaminants, due to its non-toxicity, reliable stability, and low cost [5–7]. With a relatively narrow band gap of ca. 2.7 eV, and suitable conduction and valence bands, g-C_3N_4 is appropriate for harvesting UV–vis light for the degradation of organic pollutants [8,9]. However, the rapid recombination of charge carriers, poor visible-NIR light utilization, as well as low specific surface area seriously restricts its photocatalytic activity [10]. To overcome these issues, various strategies have been attempted to improve the photocatalytic performance of g-C_3N_4, including the fabrication of micro- and nanostructures [11], coupling with metals [1,12], doping with non-metallic elements [7,13], and compositing with other semiconductors [14,15]. Remarkably, the photocatalytic activities of g-C_3N_4 may be significantly improved via its coupling with non-metallic and metals as co-catalysts [16,17]. Recently, carbon materials, such as carbon nanotube, graphene, graphene quantum dots, and carbon quantum dots, have received extensive attention because of their superior optical and electrical property

* Corresponding author.
E-mail address: liugg615@163.com (G. Liu).

http://dx.doi.org/10.1016/j.apcatb.2017.09.055
Received 16 August 2017; Received in revised form 13 September 2017; Accepted 24 September 2017
Available online 25 September 2017
0926-3373/ © 2017 Elsevier B.V. All rights reserved.

[16,18]. Carbon quantum dots (CQDs), a novel carbon nanomaterial with dimensions ranging of from 2 to 10 nm, have attracted a great deal of attention due to its non-toxicity, up-conversion capacity, and excellent electron transfer properties [19]. Owing to their unique properties, CQDs have been widely applied to improve photocatalytic performance [4,13,20–22]. More recently, Zhang et al. [23], Hong et al. [24] and Jian et al. [25] revealed that the introduction of CQDs onto g-C_3N_4 promoted the degradation of organic contaminants through the generation of additional reactive species (RSs). Our previous research has revealed that the photocatalytic activity of g-C_3N_4 for the degradation of pharmaceutical and personal care products (PPCPs) was remarkably improved following the loading of CQDs. Meanwhile, we found that this enhancement may be attributed to up-converted photoluminescence (PL) properties, efficient charge separation, and band gap narrowing of the CQDs [26].

It is generally accepted that the introduction of noble metal nanoparticles (e.g., Ag, Au, and Pt) onto semiconductor surfaces contributes to expanding the light-harvesting scope of visible-NIR light, due to their potent surface plasmon resonance (SPR) effects [17]. Further, owing to their low Fermi levels, noble metal nanoparticles might serve as electron trappers, thereby reducing the photogenerated electron-hole recombination rate [27]. Among the noble metals, Ag is considered to be the most economical raw material with the strongest SPR effect [28]. Recently, Ag loaded g-C_3N_4 catalysts have been extensively applied for enhanced photocatalytic H_2 generation [1], the photodegradation of dyes [2,17], photocatalytic disinfection [29], and remediation of PPCPs [30]. However, the atomic efficiency remains very low as only the surface atoms of the Ag nanoparticles are involved in the photocatalytic process [31]. In addition, the large size of the Ag nanoparticles would decrease the total surface area of g-C_3N_4 [32]. Therefore, the maximization of the atomic efficiency of Ag is highly desirable.

Recently, single atom-dispersion has been shown to be an effective technique for maximizing the efficiency of Ag atoms [33]. Chen et al. [32] employed silver tricyanomethanide (AgTCM) as a reactive comonomer to create a hybrid between single atom-dispersed silver and C_3N_4, which demonstrated improved performance in the selective hydrogenation of alkynes. Subsequently, Wang et al. [12] found that a hybrid single atom-dispersed Ag modified mesoporous graphitic carbon nitride showed excellent performance in the degradation of bisphenol A in the presence of peroxymonosulfate under visible light irradiation. However, to the best of our knowledge, single atom-dispersed silver and carbon quantum dot co-loading with ultrathin g-C_3N_4 (SDAg-CQDs/UCN), to form a SPR and up-converted PL synergetic system, has never been attempted.

Currently, PPCPs are commonly detected over a wide range of aquatic environments as they cannot be completely removed by wastewater treatment plants (WWTPs) [34]. The presence of PPCPs in the ambient environment can potentially impart detrimental effects on aquatic organisms and human health [35,36]. Naproxen (NPX), as one of the most commonly used non-steroidal anti-inflammatory drugs, has been widely used for the treatment of rheumatoid arthritis [37]. NPX has been frequently detected in aquatic environment with the concentrations ranging from ng L^{-1} up to μg L^{-1} [38,39]. Previous studies have demonstrated that the presence of NPX could cause harmful toxicological consequences and adverse ecological impact on the microbiological aquatic systems [40]. Therefore, it is needed to develop environmentally compatible and cost-effective treatment methods for the elimination of NPX contamination.

Herein, for the first time, we describe a strategy for the simultaneous loading of single atom-dispersed Ag and CQDs onto ultrathin g-C_3N_4 to form a synergetic SPR and up-converted PL system, which may be applied for the degradation of NPX under broad spectrum light irradiation, i.e., UV, visible, and NIR light. The structures, components, and optical properties of the hybrid were investigated via a series of characterizations. The effects of various factors including the CQDs, level of Ag loading, and light sources were investigated. The degradation of NPX under different single-wavelength LED lights was conducted in order to explore the roles of the SPR effect and up-converted PL attributes. A transformation pathway for NPX was proposed based on the detection of intermediates through liquid chromatography–tandem mass spectrometry (LC–MS/MS), gas mass spectrometry (GC–MS), and theoretical frontier electron densities (FED) calculations. Subsequently, a potentital photocatalytic mechanism for the broad-spectrum solar activity of the SDAg-CQDs/UCN was proposed. Finally, the degradation of NPX in different water matrices was examined to evaluate the technical feasibility of the SDAg-CQDs/UCN photocatalytic process for the remediation of NPX contaminated water.

2. Materials and methods

2.1. Materials

NPX (≥98%) was purchased from TCI Reagent Co. Ltd. (Shanghai China). Dicyandiamide and silver nitrate ($AgNO_3$) were obtained from Aladdin (Shanghai China). Sodium tricyanomethanide (NaTCM) was purchased from Alfa Aesar (Shanghai China). Analytical grade citric acid, ethanediamine, NH_4Cl, isopropanol (IPA), $Na_2C_2O_4$, $K_2Cr_2O_7$, benzoquinone (BQ), and sodium azide (NaN_3) were purchased from the Shanghai Taitan Technology co. Ltd. (Shanghai China). Deionized (DI) water (> 18 mΩ) was generated via a Milli-Q system. River water was obtained from the Pearl River in Guangzhou. Tap water was obtained from the Guangzhou Water Supply co. in Guangzhou. WWTPs water was collected from a sewage treatment plant (STP) in Guangzhou. Seawater was obtained from the South China Sea in Huizhou. The primary properties of the water samples were characterized and listed in Table S1.

2.2. Preparation of photocatalysts

2.2.1. Synthesis of carbon quantum dots

The CQDs were obtained via a modified hydrothermal method in accordance with the previous literature [26,41], where 1.05 g of citric acid was dissolved in 10 ml of water and 0.335 ml of ethanediamine. The mixture was then autoclaved in a Teflon container at 200 °C for 5 h. Once the sample had cooled to room temperature, the solution was centrifuged at 10,000 rpm for 20 min to remove any large particles. The obtained CQDs aqueous solution was dried at 80 °C for 24 h to produce the CQDs powder.

2.2.2. Synthesis of silver tricyanomethanide (AgTCM)

A 6 g volume of NaTCM was dissolved in 12 ml of H_2O to form solution A, whereas 9 g of $AgNO_3$ was dissolved in 18 ml of H_2O to form solution B. Subsequent to heating the two solutions to 80 °C, solution B was introduced into solution A with vigorous stirring. The mixture was then stirred overnight at room temperature. The obtained white precipitate was filtered, repeatedly rinsed with water, and then dried at 60 °C under vacuum (0.5 mbar).

2.2.3. Synthesis of SDAg-CQDs/UCN

The SDAg-CQDs/UCN was prepared via facile thermo-polymerization method, whereby 3 g of dicyandiamide, 15 g of NH_4Cl, different amounts of AgTCM (0, 0.03, 0.09, 0.15, 0.30, 0.60 g for 0, 1, 3, 5, 10, and 20 wt% of AgTCM), and different amounts of CQDs (0, 0.003, 0.0075, 0.015, 0.03, 0.06 g for 0, 0.1, 0.25, 0.5, 1.0, and 2.0 wt% of CQDs) were dissolved into 15 ml of H_2O. The mixtures were then stirred at 75 °C to evaporate the water. The resultant powder was then heated to 550 °C for 3 h at a heating rate of 2.8 °C/min. The obtained brown-yellow SDAg-CQDs/UCN powders were collected through filtration. For comparison, UCN was synthesized without the addition of AgTCM and CQDs. Further, 3 wt% SDAg/UCN and 1 wt% CQDs/UCN were synthesized by the same route.

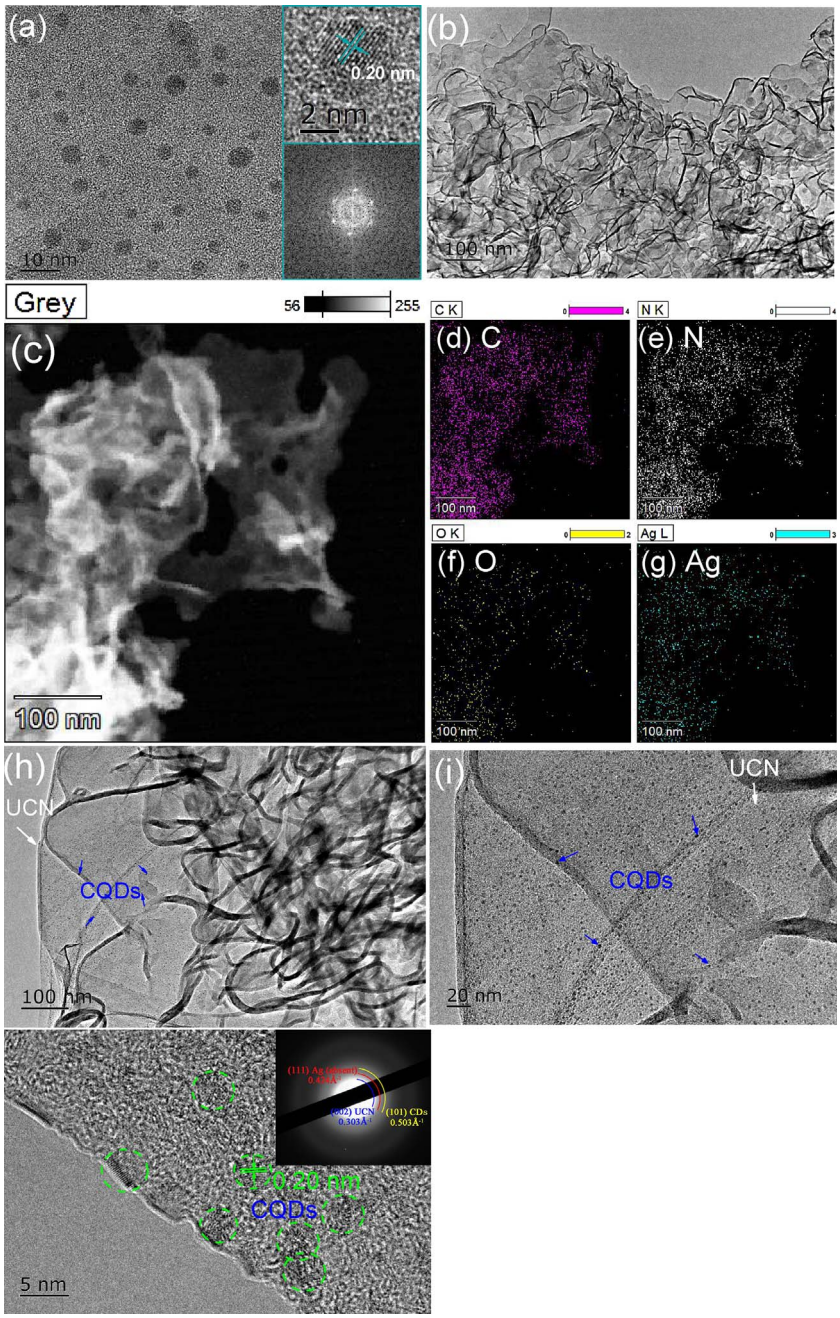

Fig. 1. (a) TEM images of CQDs. Inset shows the HRTEM of CQDs; and corresponding fast Fourier Transform (FFT) pattern; (b) TEM images of UCN; (c-g) Elemental mapping of SDAg-CQDs/UCN; (h-j) TEM images of SDAg-CQDs/UCN. Inset of (j) shows the corresponding selected area electron diffraction (SAED) patterns.

2.3. Characterization of photocatalysts

The morphology of the photocatalysts was investigated via Transmission Electron Microscopy (TEM, JEM-2100HR), which was equipped with energy dispersive spectroscopy (EDS) and high-resolution TEM (HRTEM). The XRD patterns were acquired via X-ray diffraction (XRD, BRUKER D8 ADEVANCE) with Cu Kα radiation. X-ray photoelectron spectroscopy (XPS) data was acquired using a Thermo VG ESCALAB 250 spectrometer that was equipped with Al Kα radiation (hv = 1486.6 eV). Fourier transform infrared (FTIR) spectra were recorded with a Nicolet 6700 spectrophotometer (Thermofisher). UV–vis diffuse reflectance spectra (DRS) were collected using a UV2450 UV–vis spectrophotometer (Shimadzu). Photoluminescence (PL) spectra were measured at room temperature on a FluoroMax-4 fluorescence spectrophotometer (HORIBA Jobin Yvon) with an excitation of 350 nm. Time-resolved fluorescence decay spectra were recorded by a FLS980 Fluorescence Spectrometer (Edinburgh Instruments). N_2 adsorption-desorption isotherms were measured via an Autosorb-IQ Automated Gas Sorption Analyzer (Quantachrome). Photoelectrochemical measurements were performed using a CHI660E electrochemical analyzer (CHI Shanghai, Inc.). Detailed analytical methods are conveyed in Text S1.

2.4. Photocatalytic activity tests

Photocatalytic degradation experiments were performed in a XPA-7 rotary photochemical reactor (Fig. S1, Nanjing Xujiang Electromechanical plant). A 350 W xenon lamp with 420 nm and 290 nm wavelengths was employed as the visible light and simulated sunlight sources. A monochromatic light lamp with wavelengths of 365 nm (3 W) and 740 nm (9 W, Shenzhen lamplic co., LTD.) was used as the UV light and near-infrared (NIR) light source, respectively. Furtherly, monochromatic light lamps with wavelengths of 365 nm (3 W), 450 nm (3 W), 520 nm (9 W), 660 nm (9 W), and 740 nm (9 W)

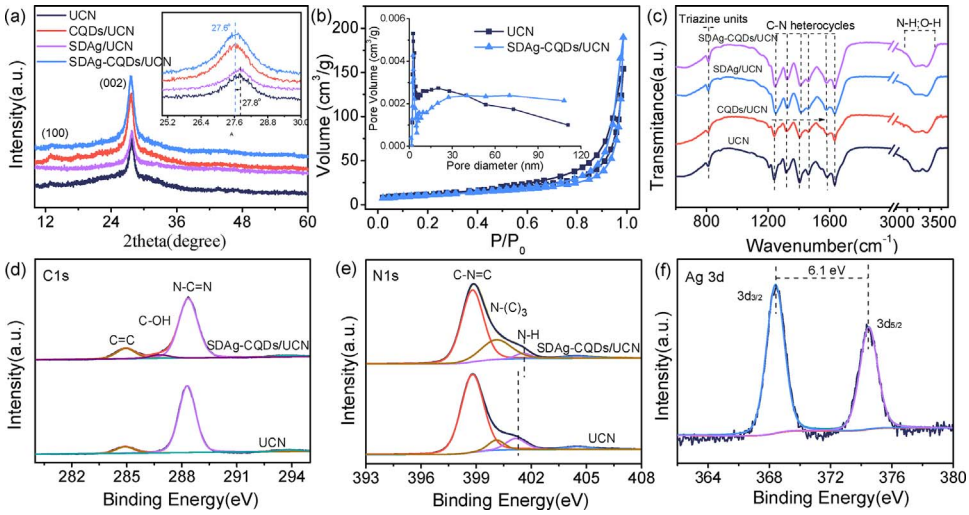

Fig. 2. (a) XRD spectrum of UCN, CQDs/UCN, SDAg/UCN, and SDAg-CQDs/UCN; (b) Nitrogen adsorption-desorption isotherms of UCN and SDAg-CQDs/UCN; (c) FT-IR spectra of UCN, CQDs/UCN, SDAg/UCN, and SDAg-CQDs/UCN; (d) High-resolution XPS spectra of C1s, (e) N1s, and (f) Ag 3d regions of UCN, and SDAg-CQDs/UCN.

purchased from Shenzhen lamplic co., LTD were used as the single wavelength light sources to investigate the roles of the SPR effect of Ag and the up-conversion function of CQDs. For each experiment, 50 mg of the photocatalyst was dispersed in 50 ml of a 4 mg/L NPX aqueous solution under magnetic stirring. Prior to irradiation, the mixture was magnetically stirred under dark condition for 30 min to ensure the attainment of adsorption-desorption equilibrium. During irradiation, a given volume of the suspension was withdrawn at a certain interval, which was filtered using 0.22 μm Millipore filters to remove the photocatalyst. The residual NPX in the solution was analyzed by LC-20A high performance liquid chromatography (Shimadzu, Japan). The photocatalytic degradation products of NPX were identified by liquid chromatography with tandem mass spectrometry (HPLC–MS/MS), and a gas chromatograph mass spectrometer (GC–MS). The detailed analytical method of HPLC, HPLC–MS/MS, and GC–MS may be found in Text S2 and Table S3. Concurrently, a TOC analyzer (TOC-V CPH E200 V, Shimadzu Co., Japan) was employed to evaluate the mineralization efficiency of the reaction solutions.

2.5. Determination of RSs during photocatalytic degradation

Electron spin resonance (ESR) spectra were performed on a Bruker JES FA200 to detect the reactive species. The spin-trap reagents were comprised of 5, 5-dimethyl-1-pyrroline N-oxide (DMPO) and 4-oxo-2, 2, 6, 6-tetramethylpiperidine (TEMP).

For the indirect analysis of the RSs, radical scavenging experiments were conducted by adding a RSs scavenger during the photocatalytic process. The scavengers used were benzoquinone (BQ, 1.0 mM) for the superoxide iron radical ($O_2\cdot^-$), isopropanol (IPA, 10 mM) for the hydroxyl radical (·OH), sodium azide (NaN_3, 75 mM) for singlet oxygens ($^1O_2$), $Na_2C_2O_4$ (10 mM) for photogenerated holes (h^+), and $K_2Cr_2O_7$ (50 μM) for photogenerated electrons (e^-), respectively.

2.6. Theoretical calculation

The frontier electron densities (FEDs) of the highest occupied molecular orbital (HOMO), the lowest unoccupied molecular orbital (LUMO), and point charge were calculated using the hybrid density functional B3LYP method, with the 6–31G(d,p) basis set (B3LYP/6-311G + (d,p)) in Gaussian 09. The optimized structure and atomic numbering of NPX is depicted in Fig. S2. Values of $FED^2_{HOMO} + FED^2_{LUMO}$, $2FED^2_{HOMO}$, and point charge were utilized to predict the reaction sites for ·OH, h^+, and $O_2\cdot^-$ attacks, respectively [20,42,43].

3. Results and discussion

3.1. Characterization

3.1.1. Morphology and composition

The TEM images in Fig. 1a display the rounded shape of the CQDs, with an average diameter of ~4 nm. The high resolution (HRTEM) image (insert) and fast fourier transform (FFT) clearly demonstrated that the CQDs exhibited a hexagonal crystalline structure with an interplanar spacing of 0.2 nm, which corresponded to the (101) lattice planes of graphite [44]. The TEM images of UCN (Fig. 1b) confirmed that the UCN had an ultrathin 2D lamellar structure. The EDS mapping of SDAg-CDs/UCN in Fig. 1c-g shows that C, N, O, and Ag were homogeneously dispersed within the UCN matrix. Further, the TEM images (Fig. 1h-j) depict the attachment of the CQDs onto the surface of the UCN. However, no Ag nanoparticles can be observed in the HRTEM image. Moreover, the inset of Fig. 1j shows that (111) diffraction ring (0.424 Å), corresponding to crystalline Ag, was absent in the selected area electron diffraction (SAED) [32]. Both HRTEM and SAED results revealed that the Ag atoms might be ubiquitously dispersed within UCN, and thereby, not in the form of nanoparticles. This result was similar to previous research [32].

The XRD patterns in Fig. 2a show two typical UCN diffraction peaks at 2θ = 27.8° and 12.9°, which may be indexed to graphitic carbon nitride, as the (002) and (100) crystal facets (JCPDS Card No. 87-1526). The stronger diffraction peak at 2θ = 27.8° with an interlayer spacing of ~0.323 nm originated from the interlayer reflection of a graphite-like crystal structure [25]. The weaker peak at 2θ = 13.0° corresponded to the in-plane structures of tri-s-triazine units [45]. Following the introduction of the CQDs, a shift in the (002) peak location, from 27.8 to 27.6° was observed (Fig. 2a inset), relating to a reduction in the stacking distance of a graphite-like plane, from 0.323 to 0.321 nm. This phenomenon might be ascribed to the compression of the CQDs nanoparticles. Nevertheless, no significant diffraction peaks of Ag were found in the SDAg-CQDs/UCN due to the small quantity and the equal dispersion of AgTCM.

N_2 adsorption-desorption isotherms of both UCN and SDAg-CQDs/UCN (Fig. 2b) exhibited type IV curves with a distinct hysteresis loop observed in the range of from 0.65-1.00 P/P_0, which reflected the mesoporous nature of the materials [3]. The BET specific surface area of SDAg-CQDs/UCN was 37.6 m^2/g, which was ca. 8.4 times higher than that of bulk g-C_3N_4 (4.49 m^2/g) [11]. In addition, the specific surface area (37.6 m^2/g) of SDAg-CQDs/UCN was slightly lower than that of UCN (57.2 m^2/g), which might be caused by the introduction of Ag and CQDs occupied a large spaces of UCN.

For the FTIR spectra of the UCN (Fig. 2c), several vibration bands at

1000–1700 cm^{-1} were attributed to the CN stretching vibrations in the CN heterocycles [29]. The band at 814 cm^{-1} originated from the vibration mode of s-triazine unit, while the broad vibration bands at 3000–3500 cm^{-1} corresponded to C-OH and N-H stretching vibrations [7]. The UCN and CQDs/UCN showed similar spectra, indicating that the loading of CQDs did not alter the chemical structure of the UCN. Whereas, following Ag doping, the stretching vibration of the CN heterocycles shifted to a higher frequency region, which might have been attributed to the increase of the force constant of the CN heterocycles, subsequent to the introduction of Ag [46].

The XPS spectra of the photocatalysts are depicted in Fig. 2d–f and Fig. S3. It can be observed that the UCN revealed the presence of C, N, and O, and Ag was found in the SDAg-CQDs/UCN in addition to the C, N, and O elements (Fig. S3a). A careful examination revealed that the surface atom ratio of carbon to nitrogen (C/N) of the SDAg-CQDs/UCN (0.686) was higher than that of the UCN (0.658), which was attributed to the introduction of the CQDs. The C1 s of UCN could be fitted to two peaks centered at 284.9 and 288.4 eV, which were identified as the characteristic peaks of C-C and sp2-hybridized carbon bonded to a N atom within the triazine rings (N—C═N), respectively [19]. For the SDAg-CQDs/UCN, a new peak at 286.8 eV was observed, corresponding to the C—OH of the CQDs (Fig. 2d and Fig. S3b). The N1 s of the UCN could be mainly divided into four peaks, with binding energies at 398.8, 400.1, and 401.15 eV, which corresponded to the sp2-hybridized N in the triazine rings (C—N═C), N-$(C)_3$, and N-H, respectively [19]. However, for the SDAg/UCN (Fig. S3c) and SDAg-CQDs/UCN (Fig. 2e), the binding energy of N-H feature increased to 401.55 eV, indicating a slight decrease in the electron density following the loading of Ag [47]. The Ag 3d spectrum of SDAg-CQDs/UCN (Fig. 2f) revealed two individual peaks at ~368.4 and 384.5 eV, with 6.1 eV splitting between the two peaks, which was assigned to the metallic Ag^0 species [12]. From the O1 s spectrum of the UCN, the peak at 532.1 and 533.5 eV were assigned to O-H and C-OH [16]. It was noted that the peak of C-OH in SDAg-CQDs/UCN was larger than that of the UCN, which might have been due to the high hydroxy group content in CQDs. In brief, both FT-IR and XPS results indicated that chemical interactions were initiated among the CQDs, Ag, and UCN.

3.1.2. Optical and electrochemical properties

The UV–vis absorption spectra in Fig. 3a depict that the CQDs demonstrated a broad absorption spectrum, with peaks centered at 240 and 342 nm, which were assigned to the typical absorptions of an aromatic π system [48]. Under 365 nm UV irradiation, a bright blue luminescence was observed, which revealed that the CQDs exhibited down-conversion fluorescent properties (Fig. 3a inset). Moreover, it may be clearly observed in Fig. 3b that CQDs had the capacity to emit photoluminescence at shorter wavelengths (379–661 nm) under longer wavelength light (550–900 nm) excitation, indicating that the CQDs possessed remarkable up-conversion fluorescent properties. The excellent optical properties of the CQDs, as a superior light harvester, might enhance the light absorption of the UCN.

The UV–vis diffuse reflectance spectra (DRS) of the UCN, CQDs/UCN, and SDAg-CQDs/UCN are presented in Fig. 3c. The UCN showed an absorption edge at ca. 473 nm, and once loaded with CQDs, the absorption edge exhibited a significant red-shift in contrast to the UCN, indicating that the CQDs may extend the visible-light spectral responsive range, from 473 to 504 nm. An intense absorption band from 500 to 800 nm was observed following the introduction of Ag. This enhancement of photoabsorption might have been attributed to the localized surface plasmon resonance (SPR) effect of the Ag [17]. The band gap energy (Eg) of the SDAg-CQDs/UCN was determined to be 2.08 eV via the Tauc approach [3], which was narrower than that of the UCN (2.62 eV) and CQDs/UCN (2.46 eV) (Fig. 3d). The narrower band gap can increase the utilization of the solar spectrum and thus promote the generation of additional electron-hole pairs under broad spectrum light [3].

In order to further investigate the photoinduced carrier separation mechanism, the energy band structures of UCN, CQDs/UCN, and SDAg-CQDs/UCN were determined by valence band X-ray photoelectron spectroscopy (VB-XPS) and Mott−Schottky plots. According to the Mott–Schottky plots (Fig. 3e), the flat-band potentials (V_{fb}) of UCN, CQDs/UCN, and SDAg-CQDs/UCN were determined to be −0.81, −0.73, and −0.62 (vs. Hg/Hg_2Cl_2 electrode), corresponding to −0.59, −0.51 and −0.40 eV (vs.NHE), respectively [49]. It was reported that the flat-band potential is approximately equivalent to the Fermi Level (E_f) for n-type semiconductors [50,51]. Hence, the Fermi levels (E_f) of UCN, CQDs/UCN, and SDAg-CQDs/UCN were −0.59, −0.51 and −0.40 eV (vs.NHE), respectively. The VB-XPS spectra (Fig. 3f) revealed that the energy gaps between the valence band (VB) and E_f were 2.28, 2.18, and 2.06 eV for the UCN, CQDs/UCN, and SDAg-CQDs/UCN, respectively [10,52]. Therefore, the VB positions for the UCN, CQDs/UCN, and SDAg-CQDs/UCN could be calculated to be 1.69, 1.67, and 1.66 eV, respectively. Simultaneously, the CB positions of the UCN, CQDs/UCN, and SDAg-CQDs/UCN were calculated, based on the Eg, to be −0.93, −0.79, and −0.42 eV (CB = VB-Eg), respectively. The energy band alignments of the UCN, CQDs/UCN, and SDAg-CQDs/UCN are schematically illustrated in Fig. 3g. It can be observed that the VB positions were kept almost constant following the introduction of CQDs and Ag, while significant positive shifts were observed in both E_f and CB. Accordingly, the CQDs and Ag possessed Fermi levels of E_f (CDs) = −0.08 eV and E_f (Ag) = −0.3 eV, respectively [21], which were more positive than that of the UCN. Therefore, upon the intimate contact of Ag and UCN, as well as CQDs and UCN, there was a Schottky barrier for electrons to traverse, from the UCN to the Ag and CQDs [30]. Generally, the accumulation of electrons inevitably causes the shifting of the Fermi level [51,53]. As a result, the Fermi level of UCN down-shifted to a more positive potential until an equilibrium was attained, which resulted in a shorter migration path for the photogenerated electrons [17]. Therefore, the electronic structure of SDAg-CQDs/UCN was expected to facilitate the occurrence of photogenerated carriers, and thus improve the photocatalytic performance of the materials.

Fig. 4a presents the PL spectra of UCN, CQDs/UCN, SDAg/UCN and SDAg-CQDs/UCN at an excitation wavelength of 350 nm. The UCN displayed an intense fluorescence emission peak at ca. 450 nm. Following the introduction of the CDs and Ag, the PL intensity decreased significantly, indicating the efficient separation of photo-excited electrons and holes [1]. A red-shift in the PL maximum was observed, which was associated with the decreased band gap energy of the UCN following the loading of the CQDs and Ag (Fig. 3d). Time-resolved PL decay spectra were measured to investigate the dynamic electron migration process. As shown in Fig. 4b, the lifetimes of the UCN, CQDs/UCN, SDAg/UCN and SDAg-CQDs/UCN were 1.12 ns, 1.18 ns, 1.24 ns, and 1.28 ns, respectively. The prolonged lifetime of photo-induced carriers indicated an accelerated charge transfer mechanism due to the introduction of CQDs and Ag [54]. Further, transient photocurrent generation and electrochemical impedance spectra (EIS) were utilized to elucidate the charge migration behavior. As shown in Fig. 4c, rapid photocurrent responses were observed for the UCN upon irradiation. In contrast to the UCN, CQDs/UCN, SDAg/UCN and SDAg-CQDs/UCN revealed a much higher photocurrent. Fig. 4d reveals that the arc radius of the EIS Nyquist plot of SDAg-CQDs/UCN was overwhelmingly smaller than that of UCN, indicating that the SDAg-CQDs/UCN possessed a lower resistance value for electron transfer [4]. Therefore, the separation efficiency and mobility of the photoinduced carriers of UCN was dramatically improved following the introduction of the CQDs and Ag.

In order to further investigate the roles of the SPR effect of Ag, the up-conversion function of CQDs as well as their charge transfer properties, the photocatalytic activities of the UCN, CQDs/UCN, and SDAg-CQDs/UCN toward the degradation of NPX were compared under different single wavelength light irradiation (365 nm, 450 nm, 520 nm, 660 nm, and 740 nm). As shown in Fig. 5a, following the introduction

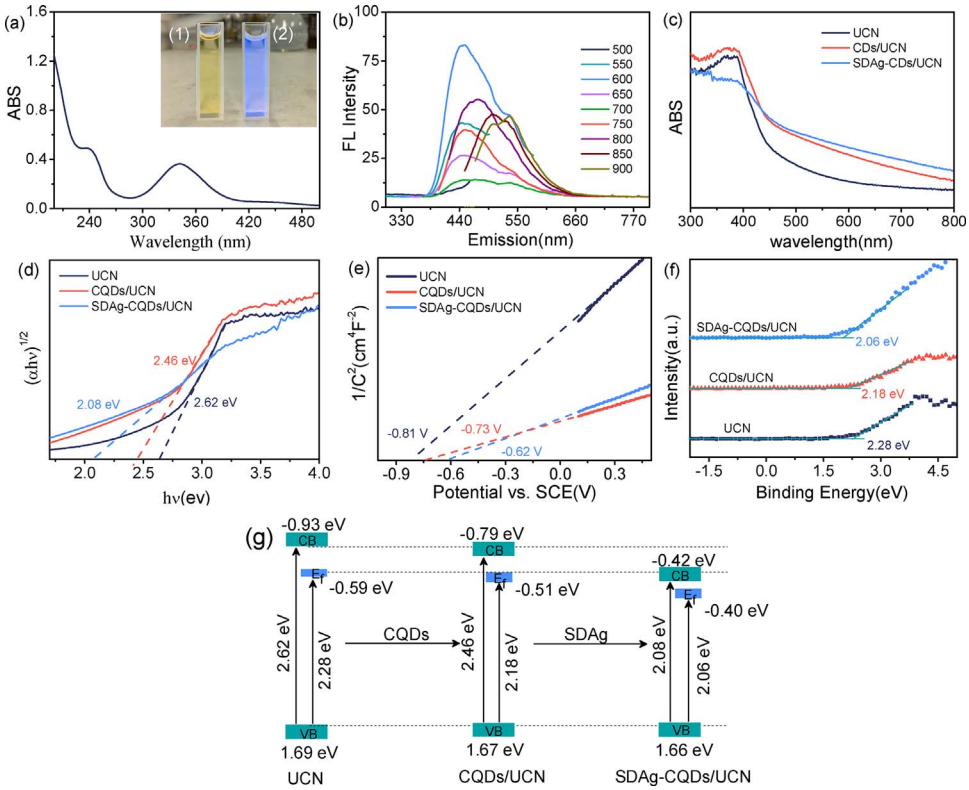

Fig. 3. (a) UV–vis absorption spectra, (b) Up-converted photoluminescence spectra of CQDs; (c) UV–vis diffuse reflectance spectra, (d) Band gaps, (e) Mott-Schottky plots, (f) VB-XPS spectra, (g) Schematic band structure evolution of UCN, CQDs/UCN, and SDAg-CQDs/UCN. Inset of (a) shows the images of CQDs solution illuminated under (1) visible and (2) 365 nm UV light irradiation.

of the CQDs, the photocatalytic activity of CQDs/UCN was significantly enhanced under all of these single wavelengths light. In order to quantitatively understand the effect of CQDs and Ag, the promotion rate was calculated following the formulas: $R_{CDs} = k_1/k_0*100\%$ and $R_{Ag} = k_2/k_1*100\%$, where R is the promotion rate, and k_0, k_1, k_2 are the rate constants of NPX in the presence of UCN, CQDs/UCN, and SDAg-CQDs/UCN, respectively. Therefore, the promotion rates of the CQDs (R_{CDs}) were calculated to be 110%, 167%, 234%, 933%, and infinity under 365 nm, 450 nm, 520 nm, 660 nm, and 740 nm irradiation, respectively (Fig. 5b). The CQDs exhibited a more significantly improved response under irradiation by longer light wavelengths. This result might have been attributed to the high up-conversion fluorescence response of CQDs under a longer wavelength of light, which was confirmed by fluorescence spectra (Fig. 3b). In addition, the loading of Ag led to practically the identical degree of enhancement, with promotion rates of 302%, 285%, and 290%, under 365 nm, 450 nm, and 520 nm irradiation, respectively. This enhanced photocatalytic activity was ascribed to the superior charge transfer properties of Ag. Interestingly, Ag demonstrated a higher degree of enhancement as the light wavelengths increased. The promotion rates of Ag were calculated to be 430% and 420% under 660 nm and 740 nm irradiation, respectively. This enhancement under long wavelength light irradiation might primarily be attributed to the SPR effect of Ag, which was confirmed by the UV-DRS spectra (Fig. 3c). The above results revealed that

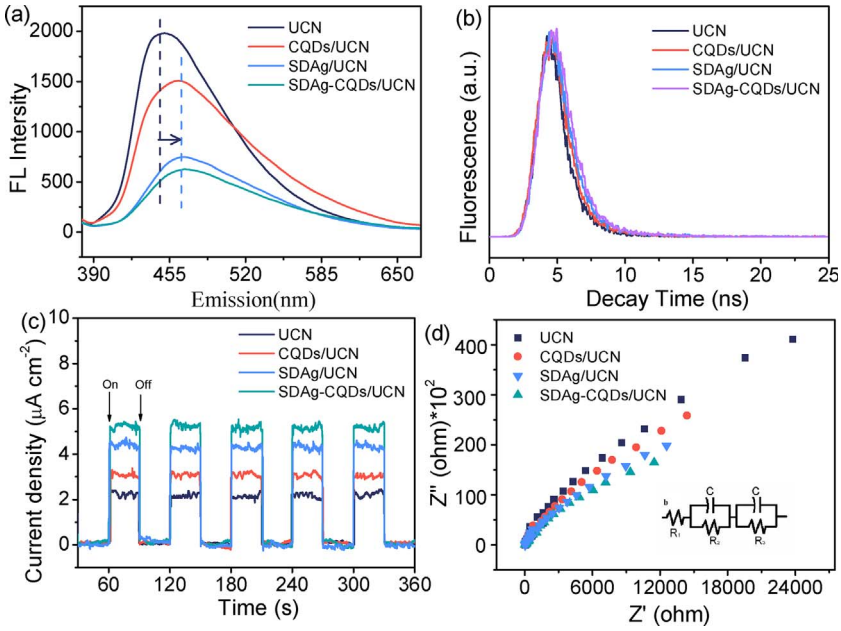

Fig. 4. (a) Photoluminescence spectra, (b) Time-resolved fluorescence spectra, (c) Transient photocurrent response, (d) Electrochemical impedance spectroscopy of UCN, CQDs/UCN, SDAg/UCN, and SDAg-CQDs/UCN.

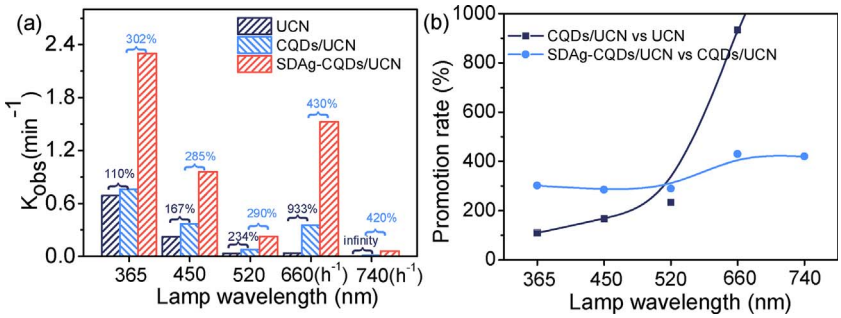

Fig. 5. (a) Kinetic rate constant of NPX over different lamp wavelengths; (b) Promotion rate of CQDs and Ag.

the SPR effects of Ag, and the up-conversion fluorescent properties of CQDs played vital roles in enhancing photoactivity and their superior charge transfer property was indispensable as well.

Based on the above results, a conclusion may be drawn that the band structure of UCN is well optimized by CQDs and Ag, which dramatically improved the photo absorbance of UCN in the visible and near-infrared regions. In addition, the superior optical and electrochemical properties of the CQDs and Ag could synergistically lead to the improvement of the photocatalytic activities of the SDAg-CQDs/UCN composite.

3.2. Photocatalytic activity of SDAg-CQDs/UCN

3.2.1. Enhanced photocatalytic activity of SDAg-CQDs/UCN

The photocatalytic performance of the as-prepared photocatalysts to degrade naproxen (NPX) under visible light irradiation was measured (Fig. 6a). The concentration of NPX demonstrated no appreciable change under 24 min of visible light irradiation, which indicated that the self-photolysis of NPX could be neglected. For the UCN, only 18.3% of the NPX was removed following 25 min of visible light irradiation. In contrast, the CQDs/UCN and SDAg/UCN composites showed significantly enhanced degradation in contrast to the UCN. The CQDs/UCN and SDAg/UCN exhibited degradation efficiencies of ca. 45.1% and 58.9%, respectively, suggesting that CQDs and Ag played a critical role in the enhancement of photoactivity. Significantly, dramatic enhancements in the degradation of NPX were observed through the simultaneous introduction of CQDs and Ag. Nearly 87.5% of the NPX was degraded over the same timeline under visible light irradiation, indicating the presence of a synergetic catalytic effect between the CQDs and Ag in the SDAg-CQDs/UCN system. Further, the SDAg-CQDs/UCN composites exhibited enhanced degradation efficiencies at 3.0, 4.5, 10.0, and infinity fold higher reaction rates than UCN under UV light, simulated sunlight, visible light, and near-infrared light irradiation, respectively (Fig. 6b). The enhanced activity of the SDAg-CQDs/UCN might have been attributed to the up-conversion fluorescent properties of the CQDs, the SPR effects of the Ag, as well as their strong charge transfer capacities. Remarkably, the SDAg-CQDs/UCN exhibited a modestly improved response under UV than for other light sources, which might have been due to the high UV absorption properties and poor up-conversion fluorescent properties of the CQDs under UV irradiation [8].

3.2.2. Effects of CQDs and Ag loading amounts on photocatalytic activity of SDAg-CQDs/UCN

Fig. 6c depicts the effects of different load volumes of CQDs on the kinetic rate constant of NPX by the SDAg-CQDs/UCN under visible light irradiation. When the quantity of CQDs was increased, from 0 to 1.0 wt %, the kinetic rate constant gradually increased, from 0.0368 to 0.0883 min^{-1}. Further increases in the loading of the CQDs to 2.0 wt% resulted in decreased photocatalytic activity. This inhibiting phenomenon might have been attributed to the photo-shielding effect of the CQDs, which occurred due to the competition for photons with the UCN [26]. Fig. 6d shows the effects of Ag content on photocatalytic activity of the SDAg-CQDs/UCN. The photocatalytic activity was initially increased, and then gradually decreased with the further addition of Ag. An Ag content of 3.0 wt% led to 2.4 and 10.0 fold higher reaction rates than those of the CQDs/UCN and UCN, respectively. The decreased photocatalytic activity with Ag content that exceeded 3.0 wt% might be attributed to the superfluous accumulation of Ag, which competed for the active reaction sites of the UCN [1].

3.2.3. Photocatalyst stability

The photocatalytic stability of the SDAg-CQDs/UCN composite was evaluated by cycling test runs for the photodegradation of NPX under visible light irradiation (Fig. 6e). Subsequent to four recycling runs, the SDAg-CQDs/UCN still exhibited good photocatalytic performance, where the NPX photocatalytic removal rate remained at ca. 82.1% after 21 min of visible light irradiation. In addition, no obvious changes in the characteristic lines were observed in the XRD, FTIR, XPS patterns of the SDAg-CQDs/UCN prior to and following four cycles (Fig. 6f–h). The above analysis indicated that the SDAg-CQDs/UCN presented the outstanding photocatalytic activity and structural stability, which was likley due to the strong chemical interactions between the CQDs, Ag, and UCN.

3.3. Discussion of underlying photocatalytic mechanisms

3.3.1. Role of reactive species

The electron spin resonance (ESR) technique with DMPO was carried out to examine the reactive species (RSs) that were generated during the SDAg-CQDs/UCN photocatalytic process. As shown in Fig. 7a–c, negligible ESR signals were observed under dark conditions. However, the four-line characteristic ESR signal for DMPO-$O_2\cdot^-$, a signal for the DMPO-·OH spin adduct, and a 1:1:1 triplet signal of the TEMP-$^1O_2$ adduct were found under visible light irradiation. This suggested that $O_2\cdot^-$, ·OH, and $^1O_2$ were generated in both the UCN and SDAg-CQDs/UCN photocatalytic systems. Moreover, all signals of the SDAg-CQDs/UCN were significantly stronger than that of the UCN, which revealed that more RSs could be generated following the introduction of CQDs and Ag. In order to quantitatively analyze the role of these reactive species, RSs trapping experiments were conducted. As shown in Table 1, the addition of NaC_2O_4 and IPA led to slight inhibitory effects toward the degradation of NPX, with inhibition rates of 11.5% and 11.1%, respectively. However, the degradation of NPX could be significantly limited when BQ, NaN_3, and $K_2Cr_2O_7$ were added, with inhibition rates of 92.5, 74.9, and 76.3%, respectively. These results indicated that $O_2\cdot^-$, $^1O_2$, and e^- played vital roles in the degradation of NPX, while ·OH and h^+ showed negligible effects. It should be pointed out that $O_2\cdot^-$ may be generated from e^- by trapping O_2, implying that e^- might participate in the degradation of NPX by generating $O_2\cdot^-$ [24]. To verify the role of O_2 during the photocatalytic process, a solution infused with N_2 and O_2 was investigated. It was observed that a higher dissolved oxygen content resulted in a more rapid degradation rate. On the contrary, the degradation of NPX was inhibited after being pumped with N_2. This result revealed that O_2 played a significant role in the photocatalytic system, and might

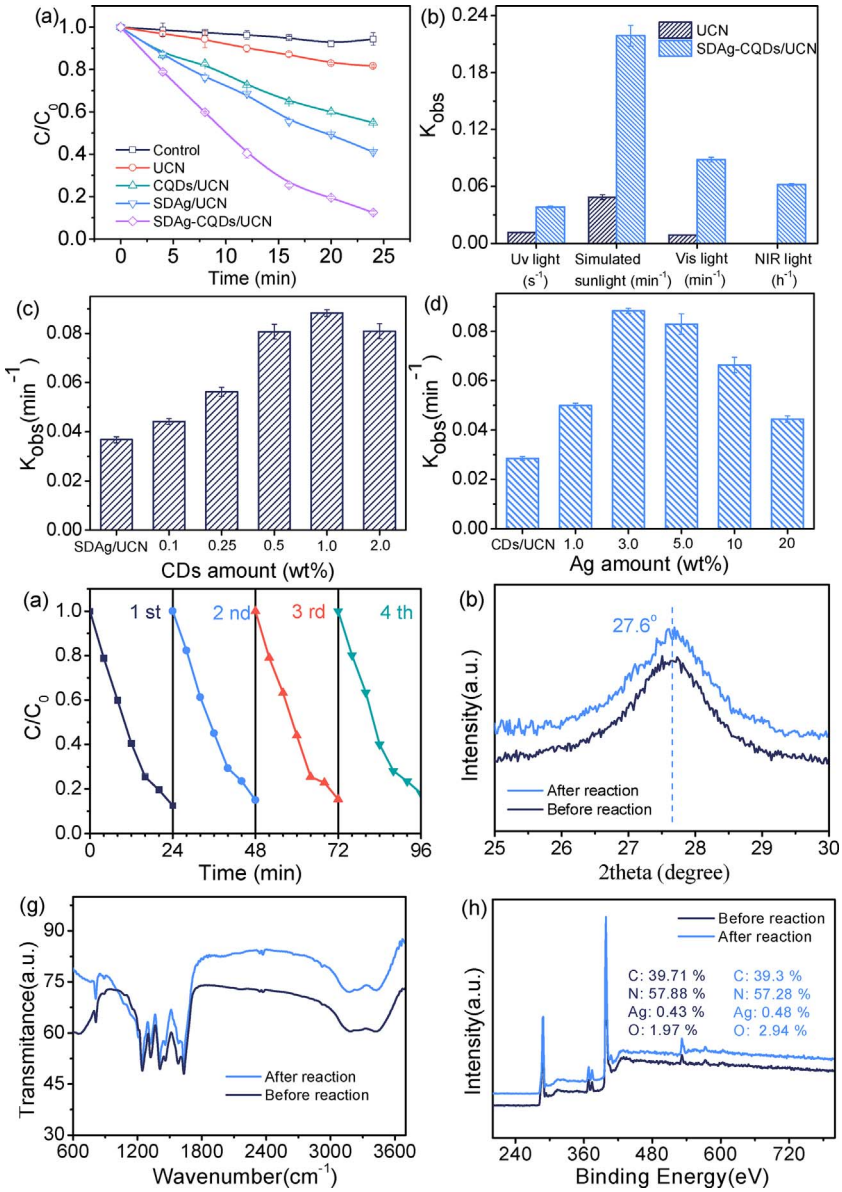

Fig. 6. (a) Photocatalytic activity of the SDAg-CQDs/UCN based on the photocatalytic degradation of NPX under visible light irradiation; (b) Kinetic rate constant of NPX over different light source irradiation, (c) loading amount of CQDs (3.0 wt% of Ag), and (d) Ag (1.0 wt% of CQDs); (e) Recycling runs of the photocatalytic activity of the SDAg-CQDs/UCN toward NPX photodegradation under visible light irradiation; (f) XRD pattern, (g) FT-IR spectra, and (h) XPS spetra of the SDAg-CQDs/UCN prior to and following repeated photocatalytic degradation experiments.

participate in the degradation of NPX by producing reactive oxygen species [8].

3.3.2. Transformation intermediates and pathways

LC–MS/MS and GC/MS techniques were carried out to identify the photocatalytic degradation intermediates of NPX. The structural elucidation of the degradation products were based on mass spectrum analysis (Tables S2 and S3; Fig. S4 to S7). Among them, intermediates with *m/z* of 158, 184, 200, 202, and 218 were assigned as the decarboxylation products of NPX. The *m/z* 262 was identified as the dihydroxylation product. Products with *m/z* 134, 148, 178, and 208 proved to be the ring opening products of NPX.

The TOC removal rates of NPX were subsequently examined to assess the extent of mineralization during the SDAg-CQDs/UCN photocatalytic process [55]. As shown in Fig. S8, following 24 min of visible light irradiation, where ca. 52.1% of TOC removal was observed, and 65.2% of TOC was removed following protracted irradiation (96 min). These results indicated that NPX and its degradation intermediates might be further decomposed by RSs, giving rise to the ring opening, and finally mineralization to CO_2 and H_2O.

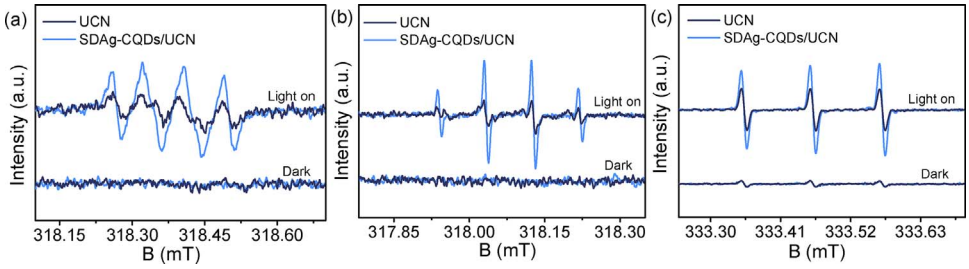

Fig. 7. (a) ESR spectra of the (a) DMPO-$O_2\cdot^-$ adducts, (b) DMPO-·OH adducts, and (c) TEMP-$^1O_2$ adduct, recorded with the UCN and SDAg-CQDs/UCN under visible light irradiation.

Table 1
Scavengers used, RSs quenched, and rate constants with quenched reactive species.

Quencher	RSs Quenched	Kobs (min^{-1})	Inhibition rate/%
Blank	\	0.0883	0
BQ	$O_2\cdot^-$	0.0066	92.5
NaN_3	$^1O_2$ + ·OH	0.0221	74.9
$K_2Cr_2O_3$	e^-	0.0209	76.3
IPA	·OH	0.0785	11.1
$Na_2C_2O_4$	h^+	0.0781	11.5
N_2	O_2	0.0317	64.1
O_2	\	0.1120	−26.8

In order to correctly identify the primary reactive sites for RSs attack, theoretical calculations were carried out based on the computation of the frontier electron densities (FEDs) and atom point charges. According to Frontier Orbital Theory, the positions with higher FED^2_{HOMO} + FED^2_{LUMO} values were more easily attacked by $^1O_2$ and ·OH, while positions with higher FED^2_{HOMO} values were more susceptible to h^+ attack [42,56]. Further, $O_2\cdot^-$ typically attacked sites with a more positive point charge [8]. As shown in Table S4, C(22) revealed a more positive point charge than others, indicating that the C(22) are likely to be attacked by $O_2\cdot^-$. Additionally, C(10) and C(1) atoms showed higher FED^2_{HOMO} values, which implied that C(10) and C(1) might be preferentially attacked by h^+. C(2), C(5), C(6), and C(9) revealed higher FED^2_{HOMO} + FED^2_{LUMO} values, indicating that the naphthalene ring of NPX was likely to be attacked by $^1O_2$ and ·OH. In fact, decarboxylation and hydroxylation products were detected by LC–MS/MS and GC/MS techniques, indicating that the prediction of possible reactive sites were quite consistent with the LC–MS/MS and GC/MS results.

On the basis of intermediate identification and reactive site prediction, the NPX degradation pathways were proposed. As shown in Fig. 8, two primary pathways, including hydroxylation and decarboxylation reactions, were involved in the photocatalytic degradation of NPX. The prediction of possible reactive sites showed that the naphthalene ring of NPX was likely to be attacked ·OH. Therefore, pathway I presents the electrophilic adduct reaction with ·OH attacking the naphthalene ring, giving rise to the formation of hydroxylation products *m/z* 262 [57]. Pathway II was initiated by $O_2\cdot^-$ attacking on the most positive point charge C(22) atom, leading to the cleavage of carboxyl, thereby giving rise to carbon centered radicals T1. Subsequently, T1 may be further oxidized by $O_2\cdot^-$ and $^1O_2$ to form *m/z* 184, 200, and 218 [58]. T1 can also react with ·OH to form *m/z* 202, which further oxidizes RSs to form *m/z* 200 [59]. Another decarboxylation reaction takes place via h^+ attack on the C(1), leading to the formation of *m/z* 158. Finally, the ring opening would occur to give rise to ring opening products *m/z* 134, 148, 178, and 208, which are finally oxidized to CO_2 and H_2O.

3.3.3. Photocatalytic mechanism

On the basis of the experimental results above, the potentially enhanced photocatalytic mechanisms in the SDAg-CQDs/UCN composite was proposed (Fig. 9). Under sunlight irradiation, electron-hole pairs were photogenerated on the surface of the UCN by absorbing UV and visible light with wavelengths of less than 473 nm. Owing to the effects of Ag and CQDs, which facilitated the accumulation of electrons, the Fermi level of the UCN was significantly down-shifted, thereby expanding the light absorption of UCN, from 473 to 504 nm. In addition, the SPR effect of Ag further promoted the light-harvesting capacity at > 500 nm light wavelengths. Meanwhile, due to the up-converted PL properties of the CQDs, long wavelengths (> 550 nm) of light could be up-converted to shorter wavelengths, which were subsequently absorbed by the UCN. The photogenerated electrons in the CB were then entrapped by Ag and CQDs due to their superior charge transfer properties, which resulted in the efficient separation of electrons and holes [21]. As the work function of Ag (4.2 eV) was lower than that of the CQDs (4.7 eV), photogenerated electrons in the UCN tended to initially transfer to Ag, and later to terminal reservoir CQDs [21,60,61]. Subsequently, the electrons on the CQDs combined with molecular oxygen to form $O_2\cdot^-$, which could react with h^+ to generate $^1O_2$. Further, $O_2\cdot^-$ can also react with H^+ to produce additional ·OH. Remarkably, because the VB position of the SDAg-CQDs/UCN was more negative than the standard redox potential of OH-/OH, h^+ were unable to oxidize OH^- and H_2O to form.OH. This was the reason behind the low ·OH content. Due to the high surface area of the SDAg-CQDs/UCN, and the π–π interactions between the NPX and SDAg-CQDs/UCN, NPX was readily absorbed onto the surface of the SDAg-CQDs/UCN. Finally, the NPX was attacked by RSs ($O_2\cdot^-$, h^+, $^1O_2$, ·OH), leading to decomposition and mineralization.

3.4. Photocatalytic degradation in different water matrices

In order to assess whether the SDAg-CQDs/UCN photocatalytic system might be applied to the decomposition of NPX under ambient conditions, the degradation of NPX was performed in different water matrices. As shown in Fig. S9, compared to DI water (87.5%), a slight inhibition was observed for the decomposition of NPX in Pearl River water (76.0%), tap water (77.8%), WWTP water (76.8%), and South China Sea water (78.5%). This inhibition might be attributed to the high concentration of water constituents (such as dissolved organic matter, HCO_3^-, transition metals, etc.), which could compete for the RSs, or weaken the radiant flux that was required for the SDAg-CQDs/UCN [62]. The results indicated that the SDAg-CQDs/UCN may be effectively utilized for the degradation of NPX under ambient water conditions.

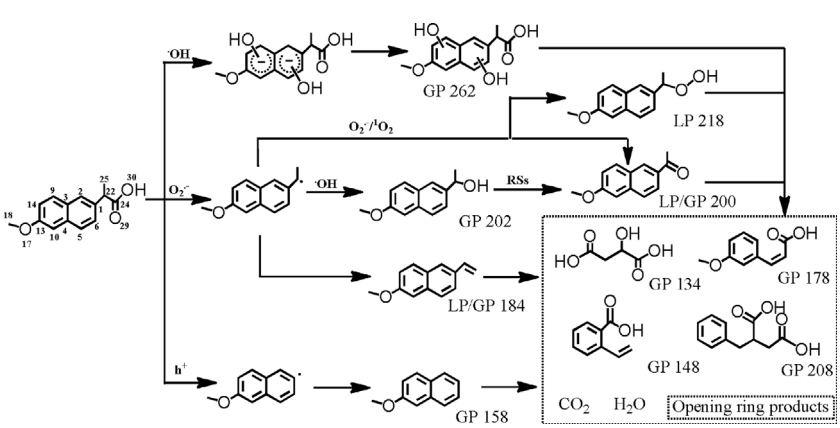

Fig. 8. Possible transformation pathways of NPX in the aqueous SDAg-CQDs/UCN solution under visible light irradiation.

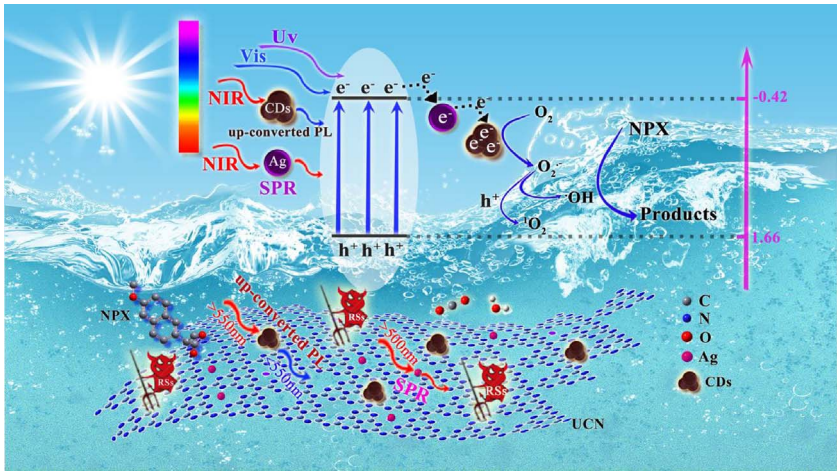

Fig. 9. Schematic photocatalytic mechanism for the SDAg-CQDs/UCN under broad- spectrum light irradiation.

4. Conclusions

In summary, we successfully fabricated, for the first time, a single-atom-dispersed silver and carbon quantum dot co-modified ultrathin g-C_3N_4 via a thermo-polymerization method. Compared with pristine UCN, CQDs/UCN and SDAg/UCN, and SDAg-CQDs/UCN exhibited significantly enhanced photocatalytic performance in the degradation of NPX under UV, Vis, and NIR irradiation. The degradation reaction rate of the SDAg-CQDs/UCN was 10 fold higher than that of the UCN. It was demonstrated that the narrowed energy gap, SPR effects of the Ag, up-converted PL properties of the CQDs, as well as their electron separation and transfer capacity, were responsible for the drastically enhanced photoactivity, as evidenced by the experimental results. The ESR technique and reactions in the presence of radical quenchers indicated that $^1O_2$ and $O_2\cdot^-$ were the dominant active species for the oxidization of NPX. The identification of transformation intermediates and reactive site prediction revealed that the NPX was finally transformed into CO_2 and H_2O. Reactions in different water matrices indicated that the SDAg-CQDs/UCN can be effectively used for the degradation of NPX under ambient water conditions. This study provided a novel strategy for a highly efficacious composite photocatalyst design for environmental remediation.

Acknowledgements

This work was supported by the National Natural Science Foundation of China (No.21377031 and 21677040), the Innovative Team Program of High Education of Guangdong Province (2015KCXTD007).

Appendix A. Supplementary data

Supplementary data associated with this article can be found, in the online version, at http://dx.doi.org/10.1016/j.apcatb.2017.09.055.

References

[1] J. Qin, H. Zeng, Appl. Catal. B-Environ. 209 (2017) 161–173.
[2] J. Jin, Q. Liang, C. Ding, Z. Li, S. Xu, J. Alloys Compd. 691 (2017) 763–771.
[3] N. Tian, Y. Zhang, X. Li, K. Xiao, X. Du, F. Dong, G.I.N. Waterhouse, T. Zhang, H. Huang, Nano Energy 38 (2017) 72–81.
[4] J. Zhang, Y. Ma, Y. Du, H. Jiang, D. Zhou, S. Dong, Appl. Catal. B Environ. 209 (2017) 253–264.
[5] P. Chen, F. Wang, Q. Zhang, Y. Su, L. Shen, K. Yao, Z.-F. Chen, Y. Liu, Z. Cai, W. Lv, G. Liu, Chemosphere 172 (2017) 193–200.
[6] X. Wang, S. Blechert, M. Antonietti, ACS Catal. 2 (2012) 1596–1606.
[7] Q. Liu, T. Chen, Y. Guo, Z. Zhang, X. Fang, Appl. Catal. B Environ. 193 (2016) 248–258.
[8] F. Wang, P. Chen, Y. Feng, Z. Xie, Y. Liu, Y. Su, Q. Zhang, Y. Wang, K. Yao, W. Lv, G. Liu, Appl. Catal. B-Environ. 207 (2017) 103–113.
[9] Y. Su, P. Chen, F. Wang, Q. Zhang, T. Chen, Y. Wang, K. Yao, W. Lv, G. Liu, RSC Adv. 7 (2017) 34096–34103.
[10] C. Liu, Y. Zhang, F. Dong, A.H. Reshak, L. Ye, N. Pinna, C. Zeng, T. Zhang, H. Huang, Appl. Catal. B-Environ. 203 (2017) 465–474.
[11] C. Chang, Y. Fu, M. Hu, C. Wang, G. Shan, L. Zhu, Appl. Catal. B-Environ. 142 (2013) 553–560.
[12] Y. Wang, X. Zhao, D. Cao, Y. Wang, Y. Zhu, Appl. Catal. B-Environ. 211 (2017) 79–88.
[13] M. Yan, F. Zhu, W. Gu, L. Sun, W. Shi, Y. Hua, RSC Adv. 6 (2016) 61162–61174.
[14] Y. Guo, J. Li, Z. Gao, X. Zhu, Y. Liu, Z. Wei, W. Zhao, C. Sun, Appl. Catal. B-Environ. 192 (2016) 57–71.
[15] G.Y. Li, X. Nie, J.Y. Chen, Q. Jiang, T.C. An, P.K. Wong, H.M. Zhang, H.J. Zhao, H. Yamashita, Water Res. 86 (2015) 17–24.
[16] J. Liu, H. Xu, Y. Xu, Y. Song, J. Lian, Y. Zhao, L. Wang, L. Huang, H. Ji, H. Li, Appl. Catal. B-Environ. 207 (2017) 429–437.
[17] Y. Bu, Z. Chen, W. Li, Appl. Catal. B-Environ. 144 (2014) 622–630.
[18] Q. Wang, N. Zhu, E. Liu, C. Zhang, J.C. Crittenden, Y. Zhang, Y. Cong, Appl. Catal. B-Environ. 205 (2017) 347–356.
[19] Y. Zhou, L. Zhang, W. Huang, Q. Kong, X. Fan, M. Wang, J. Shi, Carbon 99 (2016) 111–117.
[20] P. Chen, F. Wang, Z.F. Chen, Q. Zhang, Y. Su, L. Shen, K. Yao, Y. Liu, Z. Cai, W. Lv, Appl. Catal. B Environ. 204 (2016) 250–259.
[21] Z. Li, L. Zhu, W. Wu, S. Wang, L. Qiang, Appl. Catal. B-Environ. 192 (2016) 277–285.
[22] Q. Huang, X. Lin, C. Lin, Y. Zhang, S. Hu, C. Wei, RSC Adv. 5 (2015) 54102–54108.
[23] Z. Hui, L. Zhao, F. Geng, L.H. Guo, B. Wan, Y. Yu, Appl. Catal. B Environ. 180 (2016) 656–662.
[24] Y. Hong, Y. Meng, G. Zhang, B. Yin, Y. Zhao, W. Shi, C. Li, Sep. Purif. Technol. 171 (2016) 229–237.
[25] X. Jian, X. Liu, H.M. Yang, J.G. Li, X.L. Song, H.Y. Dai, Z.H. Liang, Appl. Surf. Sci. 370 (2016) 514–521.
[26] F. Wang, P. Chen, Y. Feng, Z. Xie, Y. Liu, Y. Su, Q. Zhang, Y. Wang, K. Yao, W. Lv, Appl. Catal. B Environ. 207 (2017) 103–113.
[27] Y. Yang, W. Guo, Y. Guo, Y. Zhao, X. Yuan, Y. Guo, J. Hazard. Mater. 271 (2014) 150–159.
[28] S. Ren, G. Zhao, Y. Wang, B. Wang, Q. Wang, Nanotechnology 26 (2015) 125403.
[29] S. Ma, S. Zhan, Y. Jia, Q. Shi, Q. Zhou, Appl. Catal. B-Environ. 186 (2016) 77–87.
[30] W. Zhang, L. Zhou, H. Deng, J. Mol. Catal. A- Chem. 423 (2016) 270–276.
[31] B. Qiao, J. Lin, A. Wang, Y. Chen, T. Zhang, J. Liu, Chin. J. Catal. 36 (2015) 1505–1511.
[32] Z. Chen, S. Pronkin, T.P. Fellinger, K. Kailasam, G. Vile, D. Albani, F. Krumeich, R. Leary, J. Barnard, J.M. Thomas, J. Perez-Ramirez, M. Antonietti, D. Dontsova, Acs Nano 10 (2016) 3166–3175.
[33] X. Li, W. Bi, L. Zhang, S. Tao, W. Chu, Q. Zhang, Y. Luo, C. Wu, Y. Xie, Adv. Mater. 28 (2016) 2427–2431.
[34] Y. Wang, W. Deng, F. Wang, Y. Su, Y. Feng, P. Chen, J. Ma, H. Su, K. Yao, Y. Liu, Environ. Sci. Process. Impacts 19 (2017) 1176–1184.
[35] X. Yang, R.C. Flowers, H.S. Weinberg, P.C. Singer, Water Res. 45 (2011) 5218–5228.
[36] C.I. Kosma, D.A. Lambropoulou, T.A. Albanis, Sci. Total Environ. 466 (2014) 421–438.
[37] E. Arany, R.K. Szabó, L. Apáti, T. Alapi, I. Ilisz, P. Mazellier, A. Dombi, K. Gajda-Schrantz, J. Hazard. Mater. 262 (2013) 151–157.
[38] M.L. Farré, I. Ferrer, A. Ginebreda, M. Figueras, L. Olivella, L. Tirapu, M. Vilanova, D. Barceló, J. Chromatogr. A 938 (2001) 187–197.
[39] J.L. Santos, I. Aparicio, E. Alonso, M. Callejón, Anal. Chim. Acta 550 (2005) 116–122.
[40] F. Méndezarriaga, J. Gimenez, S. Esplugas, J. Adv. Oxid. Technol. 11 (2008) 435–444.
[41] Y. Zhai, Z. Zhu, C. Zhu, J. Ren, E. Wang, S. Dong, J. Mater. Chem. B 2 (2014) 6995–6999.
[42] T. An, H. Yang, G. Li, W. Song, W.J. Cooper, X. Nie, Appl. Catal. B-Environ. 94

(2010) 288–294.
[43] T. An, J. An, Y. Gao, G. Li, H. Fang, W. Song, Appl. Catal. B-Environ. 164 (2015) 279–287.
[44] J. Liu, Y. Liu, N. Liu, Y. Han, X. Zhang, H. Huang, Y. Lifshitz, S.-T. Lee, J. Zhong, Z. Kang, Science 347 (2015) 970–974.
[45] K. Li, F.-Y. Su, W.-D. Zhang, Appl. Surf. Sci. 375 (2016) 110–117.
[46] H. Wang, Y. Liang, L. Liu, J. Hu, P. Wu, W. Cui, Appl. Catal. B: Environ. 208 (2017) 22–34.
[47] S. Guo, Y. Tang, Y. Xie, C. Tian, Q. Feng, Z. Wei, B. Jiang, Appl. Catal. B: Environ. 218 (2017) 664–671.
[48] S. Qu, X. Wang, Q. Lu, X. Liu, L. Wang, Angew. Chem. Int. Ed. 51 (2012) 12215–12218.
[49] K. Sayama, A. Nomura, T. Arai, T. Sugita, R. Abe, M. Yanagida, T. Oi, Y. Iwasaki, Y. Abe, H. Sugihara, J. Phys. Chem. B 110 (2006) 11352–11360.
[50] Y. Bai, L. Ye, T. Chen, L. Wang, X. Shi, X. Zhang, D. Chen, ACS Appl. Mater. Interfaces 8 (2016) 27661–27668.
[51] E. Gao, W. Wang, M. Shang, J. Xu, Phys. Chem. Chem. Phys. 13 (2011) 2887–2893.
[52] W. Luo, Z. Li, X. Jiang, T. Yu, L. Liu, X. Chen, J. Ye, Z. Zou, Phys. Chem. Chem. Phys. Pccp 10 (2008) 6717–6723.
[53] V. Subramanian, E.E. Wolf, P.V. Kamat, J. Am. Chem. Soc. 126 (2004) 4943–4950.
[54] J. Chen, H. Che, K. Huang, C. Liu, W. Shi, Appl. Catal. B Environ. 192 (2016) 134–144.
[55] Y. Ji, L. Zhou, C. Ferronato, X. Yang, A. Salvador, C. Zeng, J.M. Chovelon, J. Photochem. Photobiol. A Chem. 254 (2013) 35–44.
[56] H. Kim, W. Kim, Y. Mackeyev, G.-S. Lee, H.-J. Kim, T. Tachikawa, S. Hong, S. Lee, J. Kim, L.J. Wilson, T. Majima, P.J.J. Alvarez, W. Choi, J. Lee, Environ. Sci. Technol. 46 (2012) 9606–9613.
[57] D. Wojcieszynska, D. Domaradzka, K. Hupert-Kocurek, U. Guzik, J. Environ. Manage. 145 (2014) 157–161.
[58] Y.-Q. Gao, N.-Y. Gao, W.-H. Chu, Q.-L. Yang, D.-Q. Yin, RSC Adv. 7 (2017) 33627–33634.
[59] N. Jallouli, K. Elghniji, O. Hentati, A.R. Ribeiro, A.M.T. Silva, M. Ksibi, J. Hazard. Mater. 304 (2016) 329–336.
[60] N.T. Khoa, S.W. Kim, D.H. Yoo, E.J. Kim, S.H. Hahn, Appl. Catal. A Gen. 469 (2014) 159–164.
[61] J.H. He, C.L. Hsin, J. Liu, L.J. Chen, Z.L. Wang, Adv. Mater. 19 (2010) 781–784.
[62] S. Ahmed, M.G. Rasul, R. Brown, M.A. Hashib, J. Environ. Manage. 92 (2011) 311–330.